

PAPER • OPEN ACCESS

Prediction of sheared edge characteristics of advanced high strength steel

To cite this article: O Sandin *et al* 2022 *IOP Conf. Ser.: Mater. Sci. Eng.* **1238** 012034

View the [article online](#) for updates and enhancements.

You may also like

- [Crack Detection on Sheared-Edge of Ultra-High Strength Steel Sheet by Using Acid Immersion](#)
S. Azzmer, H. Jaafar, L. Tajul et al.
- [Effect of microstructural evolution and fractographic properties on hole expandability of hot rolling complex phase steel with different coiling temperature](#)
Jianzhong Xue, Zhengzhi Zhao, Zhiying Mo et al.
- [A source generation model for near-field seismic impact of coal fractures in stress concentration zones](#)
Junjun Feng, Enyuan Wang, Rongxi Shen et al.



The Electrochemical Society
Advancing solid state & electrochemical science & technology

243rd ECS Meeting with SOFC-XVIII

More than 50 symposia are available!

Present your research and accelerate science

Boston, MA • May 28 – June 2, 2023

[Learn more and submit!](#)

Prediction of sheared edge characteristics of advanced high strength steel.

O Sandin¹, S Hammarberg¹, S Parareda², D Frómeta², D Casellas^{1,2}, P Jonsén¹

¹ Division of Solid Mechanics, Luleå University of Technology, 971 87 Luleå, Sweden

² Eurecat, Centre Tecnològic de Catalunya, Unit of Metallic and Ceramic Materials, Plaça de la Ciència, 2, Manresa 08243, Spain

E-mail: olle.sandin@ltu.se

Abstract. In the present work, numerical models are developed for the shearing and cutting process of advanced high strength steel-blanks which can predict the edge morphology in the shear effected zone. A damage model, based on the modified Mohr-Coulomb fracture surface, is calibrated. To increase the predictability of the numerical models, the fracture surface is fine-tuned in areas corresponding to the stress-state of cutting, a methodology called Local calibration of Fracture Surface (LCFS). Four cutting cases with varying clearance are simulated and verified with experimental tests, showing good agreement. It is thus found that the suggested methodology can simulate cutting with adequate accuracy. Furthermore, it is found that solely using plane-stress tensile specimens for calibrating the fracture surface is not enough to obtain numerical models with adequate accuracy.

1. Introduction

Advanced High Strength Steels (AHSS) have become the dominant material choice for lightweight construction in the automotive and transport sector for its good in-service performance, manufacturability and recyclability. However, AHSS have some limitations regarding crack resistance and formability, which may trigger edge-cracking problems. The cause of the edge-cracking phenomena, that arises during forming or crash, have in several publications been traced to the damage induced by shear cutting processes used in early stages of the part manufacturing [1–6]. Numerical modelling methods serve as important tools during the product development, but the damage from shear cutting is seldom accounted for in traditional forming simulations. The commonly used forming limit diagram (FLD) defines the failure through thinning and localised necking and is extensively used for mild steels, but for damaged edges of AHSS materials failure tends to occur well before FLD criteria are fulfilled. To numerically model the shear cutting of AHSS can therefore aid in understanding and evaluating the edge-cracking in forming processes. This work presents an inverse modelling method to define material hardening and calibration of a Generalised Incremental Stress State Dependent Damage (GISSMO) failure- and damage model for an AHSS grade, based on plane stress tensile testing. Initial results of punching simulations showed deviating agreement in terms of cut edge shapes compared to experimental results. The authors of this article then developed an iterative approach of locally scaling the fracture locus in stress states corresponding to punching failure in order to obtain closer agreement to experimental edge morphology. The material investigated in this article is a



complex phase AHSS grade called CP1000HD of 1.5mm thickness, commonly used in automotive crash applications.

2. Constitutive modelling

Quasi-static tensile testing of four different specimen geometries enabled evaluation of the material properties under varying stress states. The results from the tensile testing was used for calibrating a plastic hardening model and to define a fracture locus, both to be used for the shear cutting FE-model presented in Section 3. The tensile specimen geometries were presented by Sjöberg et al. [7] and are schematically shown in Figure 1.

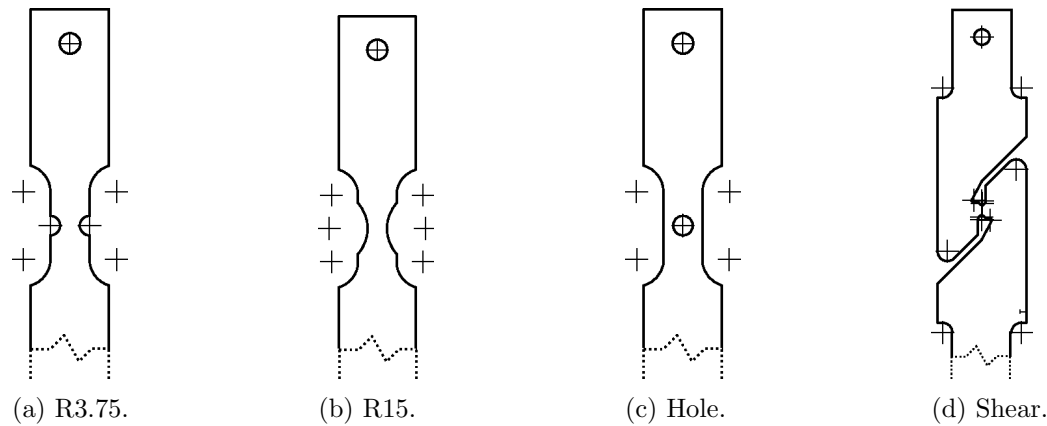


Figure 1: Tensile specimen geometries.

2.1. Plasticity

An inverse modelling scheme was used to calibrate the plastic hardening model of the CP1000HD material. The inverse modelling approach consisted of calibrating the parameters of a Stiebler hardening model such that the force - displacement results from a FE-model of the R3.75 specimen would match the corresponding experimental results. The Stiebler hardening model was described by Stiebler et al. [8] and shown in Equation (1), where parameters c_1 to c_4 were adjusted through the inverse modelling scheme shown in Figure 2. Along with the Stiebler model parameters, the Young's modulus E was calibrated. With the hardening models calibrated, a plastic hardening curve was written to an isotropic piecewise plasticity model (called MAT_24) for the FE-software LS-Dyna.

$$\sigma(\varepsilon_p) = c_1 + c_2 \varepsilon_p + c_3 (1 - \exp(-c_4 \varepsilon_p)). \quad (1)$$

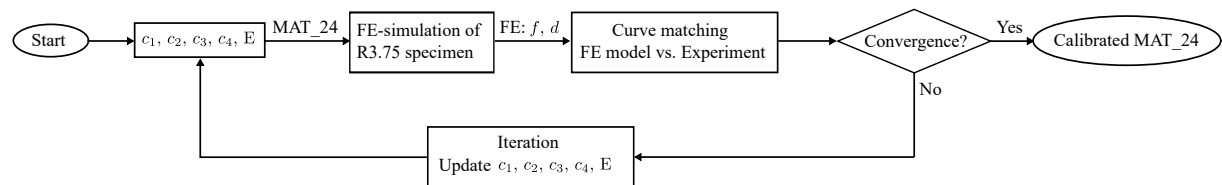


Figure 2: Calibration flowchart for the Stiebler hardening model.

2.2. Damage- and failure

In this work, modeling of damage and failure was carried out using the Generalized Incremental Stress State Dependent Damage Model (GISSMO), initially developed by Neukamm et al. [9]

and further improved by Basaran et al. [10]. GISSMO, implemented in LS-DYNA [11], is a phenomenological damage and failure model, using effective plastic strain, ϵ_{eff}^p , as a failure criteria. To account for stress-state dependent failure, the failure criterion may be expressed as a function of stress-state triaxiality, η , and lode angle parameter, $\bar{\theta}$, i.e., $\epsilon_{eff}^p = \epsilon_{eff}^p(\eta, \bar{\theta})$. Using tensor notation, the stress triaxiality and lode angle parameter may be expressed in accordance with Equations (2) and (3), where s_{ij} refers to the deviatoric part of the Cauchy stress tensor.

$$\eta = \frac{\sigma_{kk}}{3\sqrt{\frac{3}{2}s_{ij}s_{ij}}} \quad (2)$$

$$\bar{\theta} = \frac{1}{3} \arccos \left(\frac{3\sqrt{3}}{2} \frac{\frac{1}{3}s_{ij}s_{jk}s_{ki}}{(\frac{1}{2}s_{mn}s_{mn})^{3/2}} \right). \quad (3)$$

In Equation (4), the accumulative damage rule, implemented in GISSMO, is defined. \dot{D} is the incremental damage value, n is a damage exponent, $\epsilon_f(\eta, \bar{\theta})$ is the stress-state dependent failure strain, and $\dot{\epsilon}_{eff}^p$ is the increment of effective plastic strain.

$$\dot{D} = \frac{n}{\epsilon_f(\eta, \bar{\theta})} D^{(1-\frac{1}{n})} \dot{\epsilon}_{eff}^p \quad (4)$$

By coupling the damage parameter, D , to the flow stress, σ , material degradation may be modeled, see Equation (5).

$$\sigma^* = \sigma \left(1 - \left(\frac{D - D_{crit}}{1 - D_{crit}} \right)^m \right) \quad (5)$$

Initiation of the coupling between damage and stress is governed by the material instability parameter, F , accumulated according to Equation (6). At $F = 1$, the coupling to the stress is initiated. ϵ_i refers to the instability strain, which may be prescribed as a function of both stress triaxiality, η , and the lode parameter, $\bar{\theta}$.

$$\dot{F} = \frac{n}{\epsilon_i(\eta, \bar{\theta})} F^{(1-\frac{1}{n})} \dot{\epsilon}_{eff}^p \quad (6)$$

2.3. Modified Mohr-Coloumb fracture locus

From the four tensile test geometries described in Section 1, fracture strains for four unique stress-states were obtained and used for fitting a modified Mohr-Coulomb (MMC) fracture locus, first presented by Bai and Wierzbicki [12], see Equation (7). The determined values of constants $C1 - C5$ are presented in Table 1. Assuming plane stress, the lode angle parameter, $\bar{\theta}$, may be expressed as in terms of stress triaxiality, according to Equation (2.3).

$$\epsilon_f(\eta, \bar{\theta}) = \left\{ C_2 \left[C_3 + \frac{\sqrt{3}}{2 - \sqrt{3}} (C^{ax} - C_3) \left(\sec\left(\frac{\bar{\theta}\pi}{6}\right) - 1 \right) \right] \cdot \left[\sqrt{\frac{1 + C_1^2}{3}} \cos\left(\frac{\bar{\theta}\pi}{6}\right) + C_1 \left(\eta + \frac{1}{3} \sin\left(\frac{\bar{\theta}\pi}{6}\right) \right) \right] \right\}^{-\frac{1}{C_5}}, \quad (7)$$

where

$$C^{ax} = \begin{cases} 1 & \text{for } \bar{\theta} \geq 0 \\ C_4 & \text{for } \bar{\theta} < 0. \end{cases} \quad (8)$$

$$\bar{\theta} = 1 - \frac{2}{\pi} \cos^{-1} \left(-\frac{27}{2} \eta \left(\eta^2 - \frac{1}{3} \right) \right) \quad (9)$$

Table 1: MMC parameters.

Parameter	C_1	C_2	C_3	C_4	C_5
Value	0.0992	7.7814	1.0247	1.0479	0.2127

The MMC fracture locus was used as initial estimate for an inverse modelling scheme that scaled the fracture surface and calibrated the GISSMO parameters n and m . The aim of the inverse modelling was to obtain correlation between simulation and experiments in terms of material failure of the R3.75 tensile specimen. A more detailed description of the inverse modelling procedure for the hardening curve in Section 2.1 and the GISSMO damage- and failure model was given by Sandin et al. [13].

3. Numerical shear cutting models

To evaluate the effect of different tool clearances for shear cutting, two-dimensional axisymmetric FE-models of the shear cutting processes were developed in LS-Dyna. The models consisted of rigid tools (punch, die and blank holder) and the blank to which the isotropic piecewise plastic model and the GISSMO model was assigned. Spring elements were defined to model the blank holder spring and to account for the punch tool stiffness. Figure 3 shows the mesh of one of the FE-models simulated.

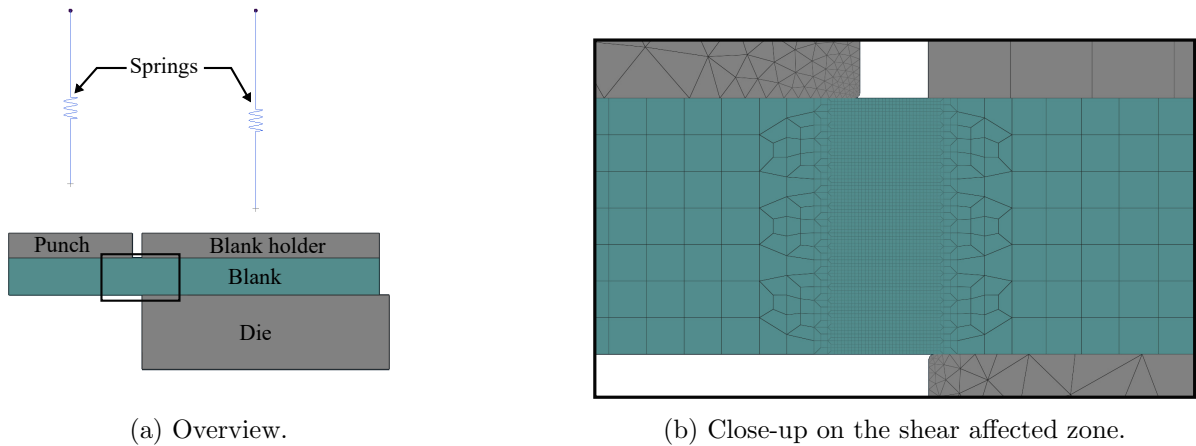


Figure 3: 2D axisymmetric FE-model setup.

Different tool clearances were obtained through horizontal offsetting of the axisymmetrical die mesh, which corresponds to changing the die diameter. Table 2 shows the tool clearance and the corresponding die radius r_{Die} for the different load cases. The variation of clearances were chosen to include both optimal industrial cutting clearances (12-20%) and the extreme cases of 5.3% and 27%. Table 3 states the geometric properties for the punching models that remained constant at all load cases, i.e. the punch diameter r_{Punch} , the blank thickness t_{Blank} , the punch edge radius $r_{\text{Punch edge}}$ and the die edge radius $r_{\text{Die edge}}$. The geometric properties of the experimental shear cutting setup were measured at the time of conducting the experiments. The tool clearance was calculated according to Equation (10).

Table 2: Clearance and corresponding die radius of the shear cutting processes.

Clearance [%]	5.267	12.133	20.533	27.000
r_{Die} [mm]	5.077	5.180	5.306	5.403

Table 3: Constant geometric properties of the shear cutting FE-models.

t_{Blank} [mm]	r_{Punch} [mm]	$r_{\text{Punch edge}}$ [μm]	$r_{\text{Die edge}}$ [μm]
1.50	4.998	30	30

$$\text{Clearance} [\%] = \frac{r_{\text{die}} - r_{\text{punch}}}{t_{\text{Blank}}} * 100 \quad (10)$$

4. Local calibration of fracture surface (LCFS)

As stated in Section 1 were initial FE-results of the shear cutting processes inaccurate in terms of cut edge morphology. The FE-results were not able to capture the crack initiation following the shearing process, why the burnish surface length was over-predicted. The inaccurate modelling results were considered to originate from the damage- and failure model described in Section 2.3, where the fracture locus consequently lacked failure data that corresponds to the stress state of interest. As the initial FE-results over-predicted the length of the burnish surface, the authors of this article could conclude that the failure strain values of the MMC surface was too large at the point of crack initiation following the burnish. In order to increase the predictability of the damage- and failure model, an iterative approach was applied of fine tuning the fracture strain in the $(\eta, \bar{\theta})$ -space corresponding to the crack initiation stress state.

Through numerical modelling of the shear cutting processes were the values of η and $\bar{\theta}$ at crack initiation identified for each cutting clearance investigated. In a Matlab script, a square box of $\pm 0.1 \epsilon_{eff}^p(\eta, \bar{\theta})$ was removed from the original MMC fracture locus around the stress state point of crack initiation and replaced with the scaled failure strain value. Continuity of the fracture locus was preserved through spline interpolation with 100 point interpolation density between the original MMC surface and the scaled failure strain value. Figure 4 shows the CP1000HD fracture locus after applying the LCFS methodology on the MMC surface presented in Section 2.3. In Figure 4 the $(\eta, \bar{\theta})$ -points corresponding to the stress state at crack initiation for different punching clearances are shown with colored dots. As the calibration points for 5.3% and 12.1% lay close to each other, the 12.1% calibration point was omitted. Figure 4 also shows the MMC plane stress failure curve defined by Equation 7, which was calibrated by the tensile tests in Figure 1. Consequently, the calibration technique means local adjustments to the original MMC failure surface in regions corresponding to crack initiation for a wide range of cutting clearances, while retaining the areas of the original MMC surface calibrated by tensile testing.

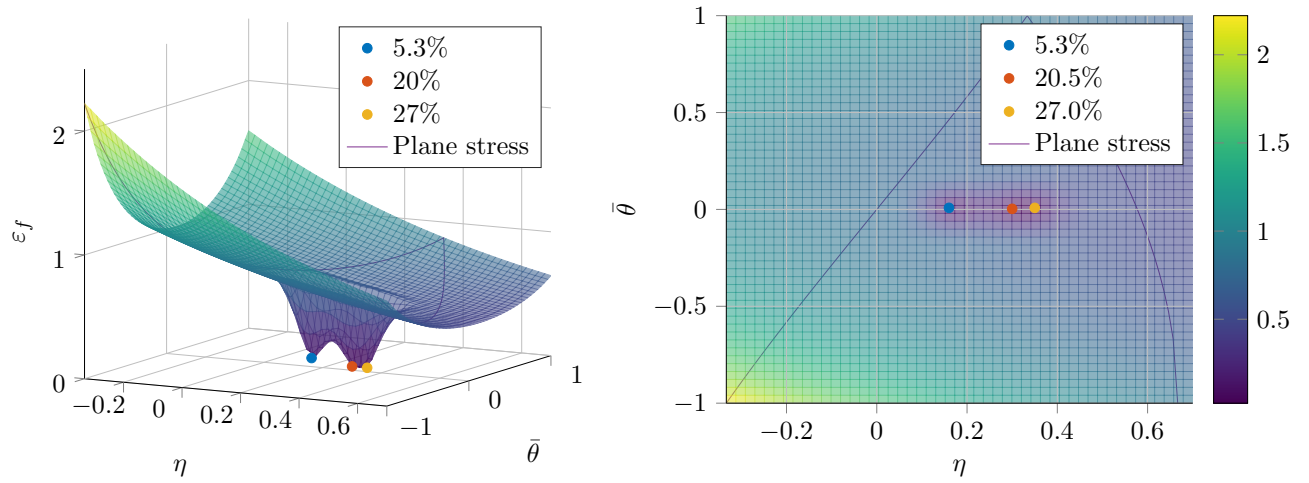


Figure 4: The fracture locus of CP1000HD after LCFS.

5. Results

In Figure 5, the cut edges from experiments and simulations are presented. Figure 5a contains the cut edge from the experiment, using a clearance of 5.3 %, and Figure 5b the corresponding simulation, using the MMC fracture locus. The simulation is able to predict the primary and secondary burnish but not the second zone of fracture, present in the experiments. Furthermore, the location of the secondary burnish deviate from experimental results. In Figure 5c, the cut edge of the simulation, using the LCFS, is presented. A closer agreement is now found between the experimental- and numerical results, as the model now predicts two burnish zones and two fracture zones, approximately at the correct locations.

In Figure 5d, the experimental cut edge, using a clearance of 12.1 % is presented, whereas Figures 5e and 5f contain the corresponding simulations, using the MMC surface and the LCFS, respectively. The effect of the LCFS is evident, as it predicts burnish and fracture zones agreeing with the experiments, whereas the model using the regular MMC does not.

Further increase of clearance, to 20.5 and 27 %, reduces predictability of the simulations using the regular MMC, seen in Figure 5g and 5h, as well as Figures 5j and 5k. For both clearances, the numerical models based on the LCFS produce cut edges in closer agreement with experimental data, see Figure 5g and 5i, as well as Figures 5j and 5l. Table 4 shows the percentual distribution of the cut edge zones over the blank thickness from experiments, as well as comparison with numerical results from cutting simulations with both original MMC failure model and calibrated failure model using LCFS.

Table 4: Cut edge zones from experiments and numerical modelling, expressed in terms of percentual distribution of the cut edge zones over the blank thickness. Numerical results are presented as results from original MMC failure model and from calibration using LCFS, separated by a forward slash symbol.

Clearance	Roll over [%]		Burnish [%]		Fracture [%]		Burr [%]		2nd burnish [%]	
	Exp.	MMC/LCFS	Exp.	MMC/LCFS	Exp.	MMC/LCFS	Exp.	MMC/LCFS	Exp.	MMC/LCFS
5.3%	3.6	2.9/2.9	22.4	47.4/48.6	22.9+20.9	16.1/16.0	0.9	0.7/0.7	30.2	33.6/32.5
12.1%	6.3	5/4.8	17.0	42.9/19.3	76.7	52.1/75.9	-	0.3/0.7	-	-
20.5%	9.4	8.2/8.1	19.7	91.8/21.0	70.9	-/70.9	-	18.7/4.9	-	-
27.0%	10.9	11.9/8.5	22.0	88.1/20.6	67.1	-/70.9	-	22.7/6.5	-	-

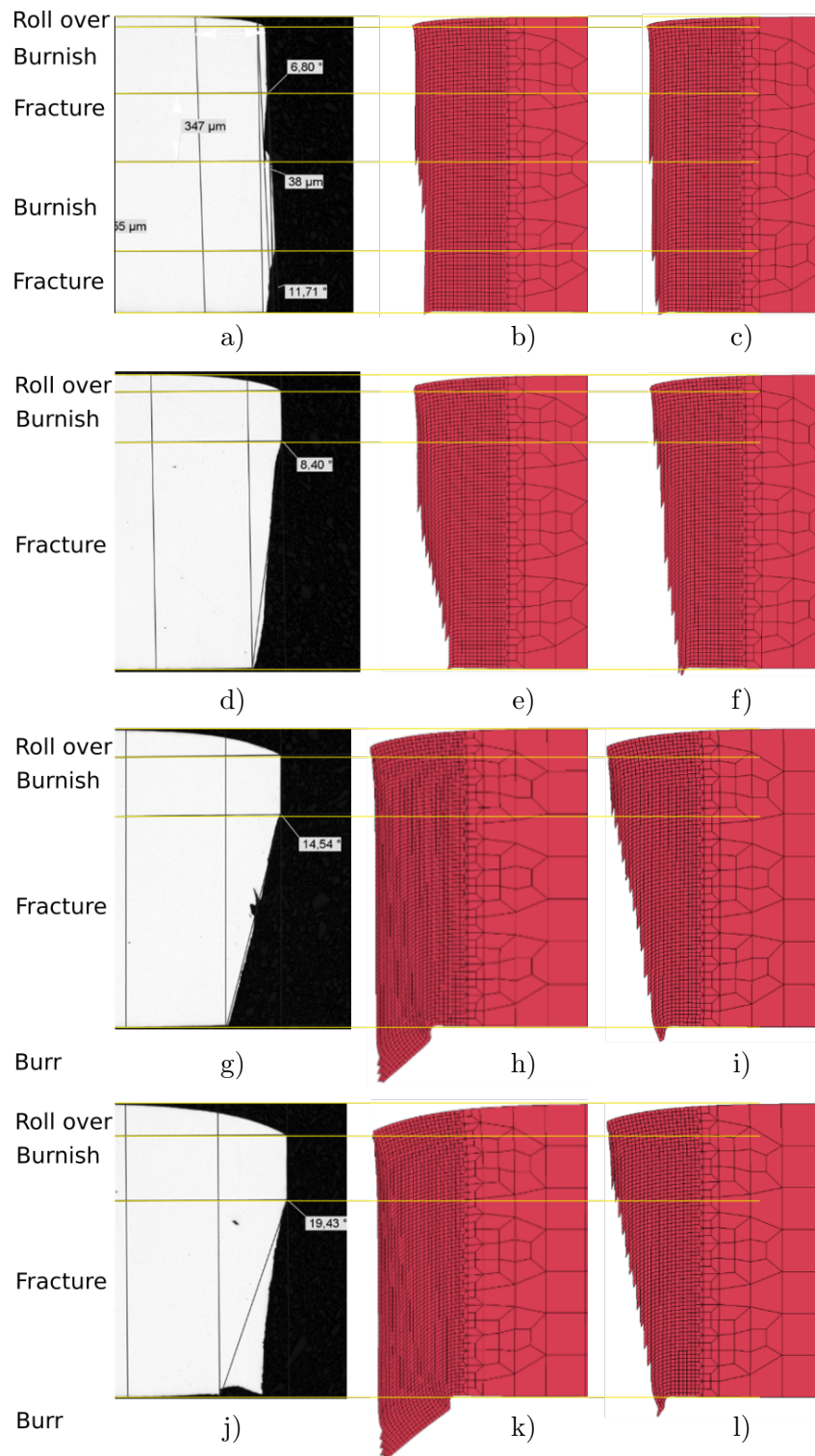


Figure 5: Cut edges from experiments and simulations are compared. Rows correspond to clearances of 5.3, 12.1, 20.5 and 27 %, respectively. In each row, the experiments are compared with simulated cut edges for the original and scaled failure surface, respectively.

6. Discussion and conclusions

The results presented in Figure 5 shows that utilisation of LCFS on the MMC fracture locus yields improved modelling results in terms of cut edge morphology. The enhanced modelling accuracy of LCFS is emphasised as it improves the modelling results for a large variation of punching clearances, ranging from 5.3% to 27.0%. As was done in this article, comparing experimental and numerical cut edge results by a single cross section, shows the possibility to improve the modelling results using LCFS. However, further work should the comparison between experimental and numerical cut edge results include effects from the circumferential variation often present in hole punching. The circumferential variation is caused by multiple factors such as orthotropic material behaviour, non-coaxial tool alignment and uneven tool ware.

However, the LCFS methodology can also be considered as a consequence of deficient calibration of the fracture locus. The inverse calibration procedure of the CP1000HD GISSMO model presented in Section 2.3 utilised a MMC fracture locus, which in turn was calibrated based on plane stress DIC measurements from tensile testing. Considering the stress state identification mentioned in Section 4 and shown in Figure 4 it can be concluded that the stress state corresponding to crack initiation during punching is not on the plane stress curve and rather found in the plane strain valley under mixed shear/uniaxial tension. The inverse modelling of the GISSMO model regarding correlation to the R3.75 tensile testing might furthermore impair the punching modelling accuracy, as the failure model risks to be sub-optimized towards a stress state not comparable to punching.

Ideally would the calibration of the MMC fracture locus include failure data from stress states corresponding to the different stages of the shear cutting process. However, such calibration experiments are particularly challenging for thin sheets as few experimental procedures exists that can control both triaxiality and lode angle at material failure and that represents the plain strain condition that prevails during hole punching. Traditionally have this kind of triaxiality/lode angle testing used both tensile testing of thin sheets and solid cylindrical specimens under compression, as presented by Bai and Wierzbicki [12, 14]. The results from the LCFS procedure can therefore aid in calibration of failure models where punching-like stress states are unable to be generated experimentally.

Acknowledgments

The authors are grateful for the contribution by Dr. Patrick Larour and Ing. Josef Hinterdorfer at voestalpine Stahl GmbH for providing experimental results of cut edges and for providing the sheet steel on which the numerical model was based. This research was partially funded by the European Commission, Research Fund for Coal and Steel, under grant agreement 847213 and the results are part of the CuttingEdge4.0 project.

References

- [1] Konieczny A and Henderson T 2007 *SAE Tech. Pap. 2007-01-0340* pp 1–12
- [2] Shih H C, Chiriac C and Shi M F 2010 *ASME Int. Manuf. Sci. Eng. Conf. MSEC 2010* **1** p 599–608
- [3] Dykeman J, Malcolm S, Yan B, Chintamani J, Huang G, Ramiseti N and Zhu H 2011 *SAE Tech. Pap. 2011-01-1058* pp 1–10
- [4] Thomas D J 2013 *J. Fail. Anal. Prev.* **13** pp 451–462
- [5] Sigvant M, Falk J and Pilthammar J 2017 *J. Phys. Conf. Ser.* **896**
- [6] Frómeta D, Tedesco M, Calvo J, Lara A, Molas S and Casellas D 2017 *J. Phys. Conf. Ser.* **896**

- [7] Sjöberg T, Marth S, Kajberg J and Häggblad H-Å 2017 *Eur. J. Mech. A/Solids* **66** pp 279–286
- [8] Stiebler K, Kunze H-D and El-Magd E 1991 *Nucl. Eng. Des.* **127** pp 85–93
- [9] Neukamm F, Feucht M, Haufe A and Roll K 2008 *10th International LS-DYNA Users Conference* (Dearborn, MI)
- [10] Basaran M, Wölkerling S D, Feucht M, Neukamm F and Weichert D 2010 *LS-DYNA Anwenderforum* (Bamberg)
- [11] Livermore software technology 2020 Tech. rep.
- [12] Bai Y and Wierzbicki T 2008 *Int. J. Plast.* **24** pp 1071–1096
- [13] Sandin O, Jonsén P, Frómeta D and Casellas D 2021 *Materials* **14** p 7821
- [14] Bai Y and Wierzbicki T 2010 *Int. J. Fract.* **161** pp 1–20